Cascade of Modal Interactions in Nanomechanical Resonators with Soft Clamping

Zichao Li,[1] Minxing Xu,[1,2] Richard A. Norte,[1,2] Alejandro M. Aragón,[1]
Peter G. Steeneken,[1,2] and Farbod Alijani[1]
[1]Department of Precision and Microsystems Engineering, Delft University of Technology, Mekelweg 2, 2628 CD Delft, The Netherlands
[2]Kavli Institute of Nanoscience, Delft University of Technology, Lorentzweg 1, 2628 CJ Delft, The Netherlands

(Received 18 July 2025; accepted 3 February 2026; published 2 March 2026)

We uncover a chain of nonlinear modal interactions in softly clamped nanostring resonators. The process involves the sequential coupling of five mechanical modes, during frequency sweeps, yielding a broad nonlinear response with nearly constant amplitude. We demonstrate that soft clamping enables this cascaded energy transfer and amplifies the effective geometric nonlinearity of the driven mode by an order of magnitude. Analytical and finite element-based reduced-order models capture the key features of the coupling cascade and clarify its underlying mechanism. The phenomenon is generic in nonlinear vibrational systems and can be tailored through soft-clamping design strategies.

DOI: 10.1103/73wb-22pz

Complex behaviors across physical systems, from fluid flows to biological synchrony, often arise when a change in a system parameter triggers a cascade of interconnected phenomena [1–3]. Such cascaded interactions are not peripheral in nonlinear dynamical systems; they are central to how energy and information propagate across coupled degrees of freedom, giving rise to rich dynamical patterns and abrupt transitions [4–7].

In recent years, micro- and nanomechanical systems have served as ideal experimental platforms for exploring nonlinear dynamics, owing to their high susceptibility to large-amplitude oscillations. These systems provide access to regimes where exotic dynamical states can emerge [8–14]. A key parameter along this pathway is the coupling between vibrational modes, which can link distinct motion states and open up opportunities for frequency stabilization [15,16], energy harvesting [17,18], and frequency comb generation [19–22]. Mode coupling in a resonant mechanical system occurs when there is a substantial energy transfer rate between different vibrational modes [23]. However, to date, studies of mode coupling have predominantly focused on interactions between two modes, typically under conditions known as internal resonance [15,19,24–26]. Studies of simultaneous mode coupling involving more than two modes have been rare because realizing multiple modal interactions generally requires both commensurate frequency ratios and sufficient energy to simultaneously activate additional modes alongside the driven one.

Published by the American Physical Society under the terms of the Creative Commons Attribution 4.0 International license. Further distribution of this work must maintain attribution to the author(s) and the published article's title, journal citation, and DOI.

Here we overcome these limitations and show that cascaded modal interactions can naturally arise and be harnessed in nanoresonators with soft clamping [27–30]. Our experiments reveal that successive intermodal couplings enable quasiconstant oscillation amplitudes over a broad frequency range. To elucidate this effect, we use analytical models and finite element (FE)-based reduced-order model (ROM) simulations to quantify the coupling strengths among different mechanical modes. We demonstrate that these cascaded interactions amplify the effective Duffing constant of the resonator by more than an order of magnitude, effectively flattening the amplitude–frequency response of the driven mode. This establishes cascaded modal coupling as a powerful mechanism for both amplitude stabilization and programmable multistable responses, offering new opportunities for precision control of signal fidelity and frequency stability in nanomechanical resonators.

Our measurements are performed on Si_3N_4 nanostrings (thickness $h = 90$ nm, pre-stress $\sigma_0 = 1.06$ GPa) featuring slender support beams at the boundaries to mediate soft clamping (see Supplemental Material S1 [31]). Such designs lead to high Q factors as well as approximate integer ratio eigenfrequencies [30,37] and thus can promote efficient intermodal couplings. Figure 1(a) shows our measurement setup, with Fig. 1(b) illustrating the geometric parameters of one fabricated device. All devices have identical dimensions ($L = 200$ μm, $w = 2$ μm, and $w_s = 1$ μm), but differ in support length L_s. We note that the presence of soft-clamping supports tunes the in-plane stress in the central string [27,30].

To characterize the nonlinear dynamics of these nanostrings, we fix the chip patterned with suspended resonators to a piezo actuator that provides a harmonic base excitation in the out-of-plane direction. We use a Zurich Instruments

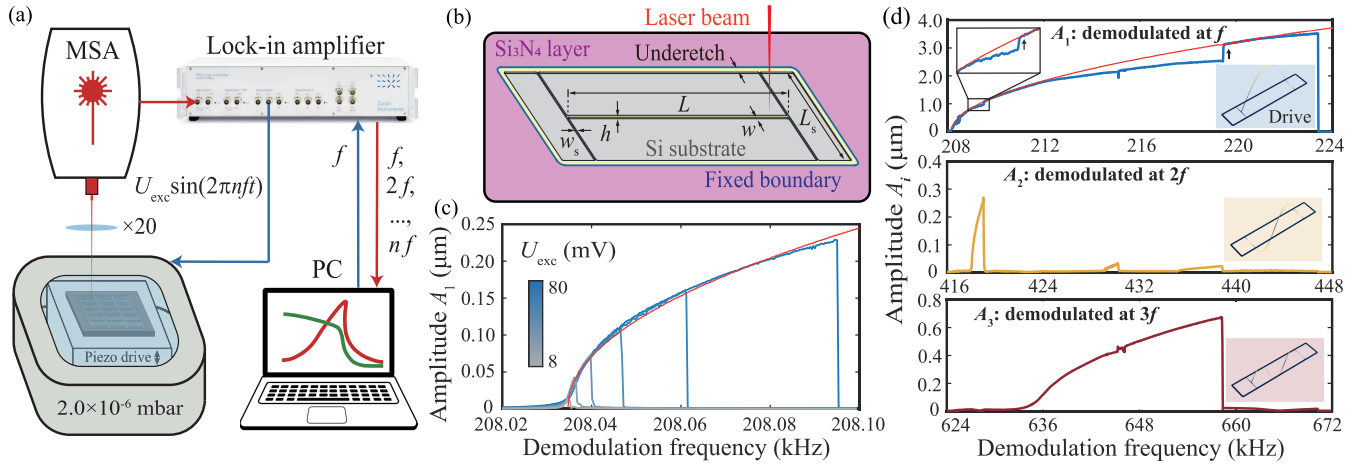

FIG. 1. Measurement of mode coupling in a nanomechanical string resonator with soft-clamping supports. (a) Schematic of the measurement setup comprising an MSA400 laser Doppler vibrometer (LDV) for reading out the motion at different harmonics of the drive frequency ($f, 2f, \ldots, nf$) and a piezo actuator for generating the excitation. (b) Geometric design parameters of a Si_3N_4 nanostring resonator with soft-clamping supports. (c) Duffing nonlinear response curves of the first mode of the device with $L_s = 50$ μm, under different drive levels without mode coupling. (d) Nonlinear response curves of the same device under a stronger drive level ($U_{exc} = 6$ V). The second (yellow) and third (ochre) modes are both activated by mode coupling. The red lines in (c), (d) (first panel) are the backbone curves of the first mode.

HF2LI lock-in amplifier to perform frequency sweeps in the spectral neighborhood of the first resonance, together with a Polytec MSA400 laser Doppler vibrometer (LDV) for detecting the out-of-plane vibrations of our devices. All modes discussed in this Letter refer specifically to out-of-plane modes. The measurement laser is focused at a position $L/12$ from the support on the central string, ensuring that it is distant from nodal points of the lowest vibrational modes (see Supplemental Material S2 [31]). We perform all measurements at room temperature in a vacuum chamber with a pressure below 2×10^{-6} mbar to minimize air damping.

To probe the geometric nonlinearity of our devices, we perform forward frequency sweeps at different drive levels and measure the vibrations of the central string [30]. As an example, Fig. 1(c) shows the frequency responses at various drive voltages, ranging from $U_{exc} = 8$ to 80 mV, for a device with $L_s = 50$ μm. To quantify the strength of nonlinearity, we use the Duffing equation,

$$\ddot{q}_1 + c_1\dot{q}_1 + \omega_1^2 q_1 + \beta_1 q_1^3 = F_{exc}\sin(2\pi f t), \qquad (1)$$

where q_1 is the generalized coordinate of the first mode and $F_{exc}\sin(2\pi f t)$ is its effective harmonic drive with excitation frequency f from the piezo. Furthermore, $\omega_1 = 2\pi f_1$, $c_1 = \omega_1/Q_1$, and β_1 are the angular resonance frequency, mass-normalized damping coefficient, and Duffing constant, respectively, where $Q_1 = 6.07 \times 10^5$ is the quality factor characterized by the ring-down measurement [27]. We extract β_1 by fitting the backbone curve [red line in Fig. 1(c)] [36,38].

In Fig. 1(d), we show the frequency response of the same device measured in Fig. 1(c) driven at a stronger excitation level ($U_{exc} = 6$ V) around the first resonance. Apart from the signal demodulated with the drive frequency f (blue), we also detect higher harmonics demodulated at $2f$ (yellow) and $3f$ (ochre). We note that the frequency response of the first mode deviates from the backbone curve of the Duffing response [red line in Fig. 1(d)] when the higher harmonics are detected. Since the resonance frequencies of higher modes of a string resonator are close to integer multiples of the first, we attribute the deviation from the backbone curve to modal interactions between the first and higher-order modes [39]. When the oscillations of the coupled modes drop, the energy stored in the higher modes transfers back to the driven mode, bringing its amplitude closer to its backbone [see arrows in Fig. 1(d)]. We provide a more detailed explanation of the multiple disconnected features that appear in the response near $2f$ in Supplemental Material S3 [31].

To further examine the amplitude jumps (arrows) and coupling conditions in Fig. 1(d), we perform a detailed investigation on the coupling between the first and second modes in a device with identical geometry, as shown in Fig. 2(a). Starting with a drive voltage of $U_{exc} = 200$ mV and a frequency step of $\Delta f = 50$ Hz, we obtain a Duffing response of the first mode without activation of the second mode. However, when we reduce Δf to 10 Hz while keeping the same drive voltage, we observe that the second mode is activated (gray area). As the drive frequency is swept forward, the oscillations of both modes drop to their respective lower amplitude branches. To further explore the influence of drive level, we double U_{exc} to 400 mV. We can see that the oscillation of the first mode is driven back to its upper stable branch at the end of the coupling regime, while

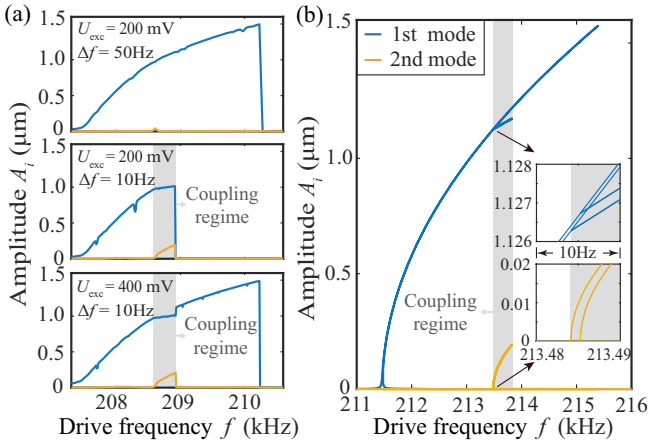

FIG. 2. Different response branches of the first mode determined by its coupling to the second mode. (a) Measured response curves by driving the first mode under different U_{exc} and Δf, showing frequency demodulation around f (blue, first mode) and $2f$ (yellow, second mode). (b) Simulated response curves based on an FE-based ROM, showing the directly driven first mode near f (blue) and the coupling-induced second mode around $2f$ (yellow). The gray area marks the frequency range where the second mode is activated.

the second mode drops to its lower branch, consistent with Fig. 1(d). This observation suggests that the driving parameters can influence the slope of the solution branches during a frequency sweep.

To verify our observation, and to study the mode coupling mechanism in a two-mode system, we employ an FE model of the nanoresonator and build a two-degrees-of-freedom (2-d.o.f.) ROM that comprises the first two modes (see previous works [30,40,41] and Supplemental Material S3 [31] for more details):

$$\ddot{q}_1 + c_1\dot{q}_1 + \omega_1^2 q_1 + \beta_1 q_1^3 + \gamma q_1 q_2^2 = F_{\mathrm{exc}} \sin(2\pi f t), \quad (2a)$$

$$\ddot{q}_2 + c_2\dot{q}_2 + \omega_2^2 q_2 + \beta_2 q_2^3 + \gamma q_1^2 q_2 = F'_{\mathrm{exc}} \sin(4\pi f t). \quad (2b)$$

Here, q_2 is the generalized coordinate of the second mode. $\omega_2 = 2\pi f_2$, $c_2 = \omega_2/Q_2$, and β_2 are its angular resonance frequency, mass-normalized damping coefficient and Duffing constant, respectively, where Q_2 is the quality factor of the second mode. We introduce a minute harmonic force $F'_{\mathrm{exc}} \sin(4\pi f t)$ to capture the influence of the quadratic coupling induced by symmetry-breaking imperfections of the device. This term is necessary to excite the second mode (see Supplementary Material S3 [31]). Moreover, γ in Eqs. (2a) and (2b) represents the mass-normalized dispersive coupling coefficient between the two modes that is directly obtained from the ROM and promotes energy transfer [23]. We use numerical continuation [42] to compute all possible solution branches of the 2-d.o.f. system, as shown in Fig. 2(b) (see Supplemental Material S6 [31]). At the onset of mode coupling we also notice the emergence of a second solution branch with a slope different from the common Duffing response in the coupling regime [43], which matches our experimental observation obtained by frequency sweeps. The simulation reveals that the amplitude of the second mode increases rapidly at the onset of mode coupling [see insets in Fig. 2(b)], implying that a coarse frequency sweep may overlook its activation window. We attribute this phenomenon to the high Q-factor of our devices and the presence of nonlinear coupling terms ($\gamma q_1 q_2^2$ and $\gamma q_1^2 q_2$), which govern the energy exchange between the modes in this 2-d.o.f. system. In subsequent experiments, we ensure sufficiently small frequency steps to reliably activate the coupled motion and trace the solution branch that emerges from the coupling.

Next, to quantify the influence of soft-clamping supports on mode coupling, we measure devices with varying support lengths L_s undergoing intermodal coupling between the lowest two modes, as shown in Fig. 3(a) (see Supplemental Material S5 [31] for more measurement results). The kinks at relatively large amplitudes signify transitions to alternative solution branches—features that closely resemble those observed in our numerical simulations in Fig. 2(b) and are indicative of extra vibrational modes becoming active through dispersive coupling.

To derive the onset conditions of a two-mode coupling, we apply the Harmonic Balance Method (HBM) (see Supplemental Material S3 [31]) to Eqs. (2a) and (2b), thereby obtaining analytical expressions that predict the frequency $f_{1,c}$ and amplitude $A_{1,c}$ of the first mode at the onset of coupling [see kinks in Fig. 3(a)]:

$$f_{1,c} = \frac{1}{2\pi}\sqrt{\frac{\omega_2^2 - \frac{2\gamma}{3\beta_1}\omega_1^2}{4 - \frac{2\gamma}{3\beta_1}}}, \qquad A_{1,c} = \sqrt{\frac{\omega_2^2 - 4\omega_1^2}{3\beta_1 - \frac{1}{2}\gamma}}. \quad (3)$$

We use Eq. (3) and parameters from FE-based 2-d.o.f. ROMs to predict the onset of coupling [see green triangles in Fig. 3(b)]. The obtained values closely match the kinks observed in response curves simulated from the same ROMs (see Supplemental Material S6 [31]). The predictions also match $f_{1,c}$ and $A_{1,c}$ extracted from experimental response curves for devices with different support lengths, as demonstrated in Figs. 3(c) and 3(d). These results confirm the validity of Eq. (3) in predicting the kink in the nonlinear frequency response curve.

Apart from the onset of two-mode coupling, we can see from Fig. 3(a) that the coupled response also has an impact on the spring-hardening nonlinearity of the driven mode. The amplitude-frequency relationship after the kinks remains parabolic, which closely tracks the effective backbone curve of the first mode undergoing dispersive coupling with the second mode (see Supplemental Material S3 [31]).

The HBM analytical framework further allows us to extend the two-mode analysis to a situation where multiple

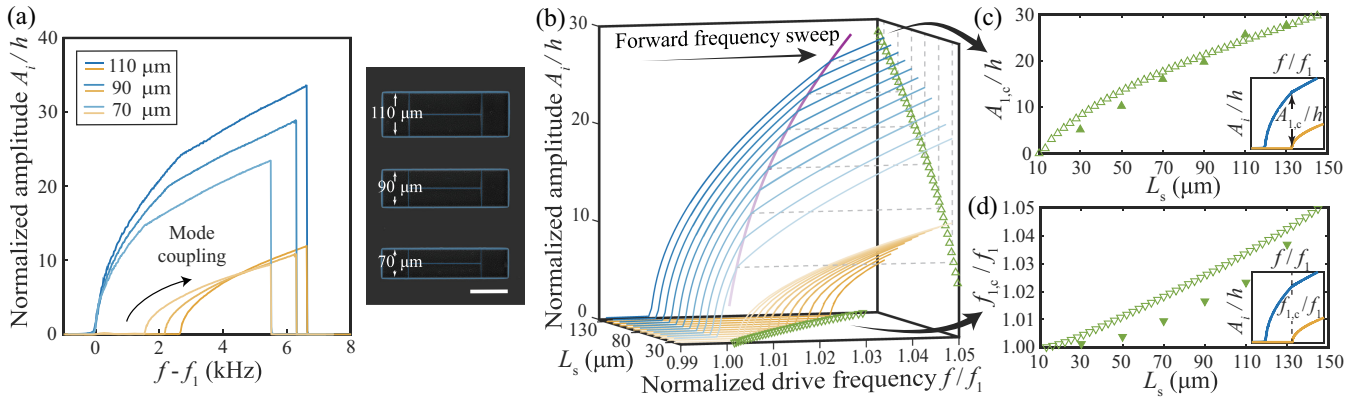

FIG. 3. Influence of the soft-clamping supports on the coupled dynamics of the lowest two modes. (a) Measured response curves of the lowest two modes of string resonators with three different L_s, showing frequency demodulation around f (blue, first mode) and $2f$ (yellow, second mode). The colors of the curves gradually fade as L_s decreases. The scanning electron microscope (SEM) image shows the measured devices (colored in blue). The white bar is 100 μm. (b) Simulated response curves using the FE-based ROMs of devices with varying L_s, showing the directly driven first mode near f (blue) and the coupling-induced second mode around $2f$ (yellow). The upward and downward hollow triangles represent the onset frequency of the coupled mode $(f_{1,c}/f_1)$ and the corresponding amplitude $(A_{1,c}/h)$, respectively, as predicted by Eq. (3). The purple line traces the onsets of modal interactions, corresponding to the kinks in the blue curves. (c),(d) Comparison of the simulated (hollow triangles) and measured (solid triangles) onset amplitude $A_{1,c}/h$ and frequency $f_{1,c}/f_1$. The insets define $f_{1,c}/f_1$, and $A_{1,c}/h$, respectively.

modes are coupled via cubic nonlinearity and excited simultaneously, in a cascadelike fashion, when only the lowest mode is driven. To that end, and in order to capture the impact of successive dispersive couplings from the interaction potential $\propto q_1^2 q_i^2$ $(i \geq 2)$ on the nonlinear dynamics of the fundamental mode, we derive a recursive relation for the effective Duffing constant as additional coupled modes are introduced (see Supplemental Material S7 [31]):

$$\beta_{1,\mathrm{eff}}^{(i)} = \frac{3}{4}\beta_{1,\mathrm{eff}}^{(i-1)} + \frac{3i^2\beta_{1,\mathrm{eff}}^{(i-1)}\gamma_{1,i} - 2\gamma_{1,i}^2}{6\beta_i - 4i^2\gamma_{1,i}}, \tag{4}$$

where $\beta_{1,\mathrm{eff}}^{(i)}$ is the effective Duffing constant by including up to the ith mode $(i \geq 2,\ \beta_{1,\mathrm{eff}}^{(1)} = \beta_1)$, β_i is the intrinsic Duffing constant of the ith mode, and $\gamma_{1,i}$ is the dispersive coupling coefficient between the first and ith modes. This relation serves as a predictive map that quantifies how successive dispersive interactions modulate the nonlinearity of the first mode, providing both physical insight and a tool for engineering multimode dispersive interactions. However, we note that this approximation neglects the interactions among the coupled modes other than the first mode and assumes that higher-order modes are activated (see Supplemental Material S7 [31]).

In Fig. 4(a), we schematically illustrate this effect: the red curve shows the reshaped backbone of the first mode's response as successive dispersive couplings are introduced. The initial segment represents the uncoupled response of the first mode. Kinks in the curve, marked by black dots, indicate changes in the slope of the Duffing response and correspond to higher-order modes coupling into the dynamics. In fact, these sharp transitions reflect how higher modes act as energy reservoirs, absorbing part of the energy injected into the first mode and thereby suppressing its vibration amplitude [7,15].

By substituting parameters extracted from FE-based ROMs for the device measured in Fig. 1, we find that incorporating two-mode coupling leads to a 52% increase in the effective Duffing constant. With interactions among five modes, the model of Eq. (4) predicts an enhancement exceeding a 26-fold increase in $\beta_{1,\mathrm{eff}}^{(i)}$ (see Supplemental Material S7 [31]).

To experimentally investigate the cascaded interactions predicted by our analytical model [Eq. (4)], we perform forward frequency sweeps on the device measured in Fig. 1 with a higher excitation level ($U_{\mathrm{exc}} = 20$ V) to activate higher-order modes. Consistent with the analytical prediction, the measured frequency response in Fig. 4(b) shows a clear suppression of the fundamental mode's amplitude, resulting in an almost constant response over a broad frequency range as higher-order modes participate in the coupled dynamics. The unstable fluctuations observed after the onset of the fourth mode are attributed to the activation of coupling to higher-order modes $(i > 6)$. To assess the validity of Eq. (4) in capturing the rescaling of the Duffing constant via modal coupling, we also performed FE-based ROM simulations including all-to-all coupling terms (see Supplemental Material S7 [31]). These simulations reveal that, while higher-order resonant interactions are present and affect the overall dynamics, the dominant dispersive terms influencing the first mode are those already included in the analytical model.

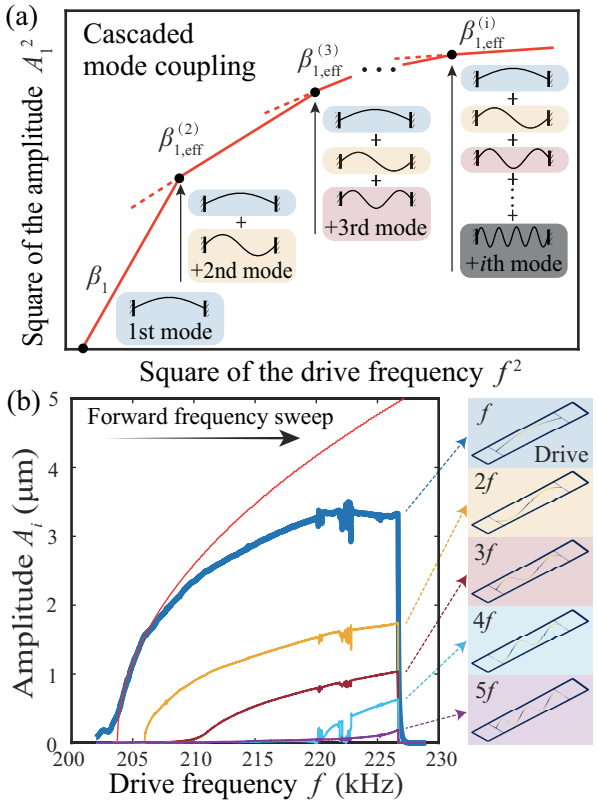

FIG. 4. Cascaded interactions in a nanostring. (a) The red line denotes the driven mode's effective backbone, with higher modes triggered at its kinks via dispersive coupling. (b) Measured response curves under five-mode couplings in the device with $L_s = 50$ μm. The bold blue line is the frequency response demodulated by the drive frequency f, while the others represent the signals demodulated by $2f$ (yellow), $3f$ (ochre), $4f$ (cyan), and $5f$ (purple), respectively. The mode shapes from FE analysis are shown on the right. The red line is the fitted backbone curve of the first mode before mode couplings initiate.

It is worth noting that, despite the significant potential of intermodal modulation, achieving multimodal coupling in most micro- and nanomechanical resonators is inherently challenging due to the incommensurate ratios of their eigenfrequencies. Soft clamping offers a key advantage in this regard: its inherent design flexibility enables precise tuning of eigenfrequency ratios. Under hardening nonlinearity, this allows for rapid access to the coupling regime during a forward frequency sweep, without the need for large vibrational amplitudes to overcome detuning. Moreover, soft clamping significantly enhances Q factor, which promotes the participation of a larger number of vibrational modes by lowering the energy threshold required to initiate modal interactions.

To summarize, we present evidence and models for cascaded intermodal couplings in resonators with soft clamping. The ability of using these cascades for exciting multiple couplings in high-Q resonators with a single drive tone not only facilitates the actuation of successive modes but also allows for reshaping and engineering the system's nonlinear dynamic response. Cascades of intermodal couplings can stabilize the amplitude of the driven mode across a broad frequency range [see Fig. 4(b)] and allow for more freedom in tuning the amplitude-frequency response than when using only two-mode couplings. This multimode nonlinear response engineering might, with more refined procedures that still need to be developed, enable amplitude and frequency stabilization, as well as potentially achieve phase noise reduction in nonlinear oscillators beyond what has been demonstrated for two-mode couplings [15,44,45]. More advanced prospects of multimode cascades involve their use for nanomechanical error correction in a single resonator, along a route that has recently been demonstrated using three separate coupled oscillators [46]. Finally, programmable multistability of all, or a subset of, cascade modes by appropriate drive control could open new opportunities for logic operations and nanomechanical computation [47–49].

Acknowledgments—This work was funded/cofunded by the European Union (ERC Consolidator, NCANTO, 101125458). Z. L. also acknowledges financial support from the China Scholarship Council and fruitful discussions with Dr. Ata Keşkekler. This work is also part of the project "Probing the physics of exotic superconductors with microchip Casimir experiments (740.018.020)" of the research program NWO start-up, which is partly financed by the Dutch Research Council (NWO). M. X. and R. A. N. acknowledge support from the Kavli Nanolab Delft.

Data availability—The data that support the findings of this article are not publicly available. The data are available from the authors upon reasonable request.

[1] S. H. Strogatz, *Sync: How Order Emerges from Chaos in the Universe, Nature, and Daily Life* (Hachette, United Kingdom, 2012).
[2] F. Gu, B. Guiselin, N. Bain, I. Zuriguel, and D. Bartolo, Nature (London) **638**, 112 (2025).
[3] A. Japaridze, V. Struijk, K. Swamy, I. Rosłoń, O. Shoshani, C. Dekker, and F. Alijani, Small **21**, 2407832 (2025).
[4] E. Lorenz, World Sci. Ser. Nonlinear Sci. A **39**, 91 (2000).
[5] R. M. May, Nature (London) **261**, 459 (1976).
[6] A. F. Vakakis, O. V. Gendelman, L. A. Bergman, A. Mojahed, and M. Gzal, Nonlinear Dyn. **108**, 711 (2022).
[7] C. Chen, D. H. Zanette, D. A. Czaplewski, S. Shaw, and D. López, Nat. Commun. **8**, 1 (2017).
[8] M. H. Matheny, J. Emenheiser, W. Fon, A. Chapman, A. Salova, M. Rohden, J. Li, M. Hudoba de Badyn, M. Pósfai, L. Duenas-Osorio *et al.*, Science **363**, eaav7932 (2019).
[9] J. Güttinger, A. Noury, P. Weber, A. M. Eriksson, C. Lagoin, J. Moser, C. Eichler, A. Wallraff, A. Isacsson, and A. Bachtold, Nat. Nanotechnol. **12**, 631 (2017).
[10] A. Keşkekler, O. Shoshani, M. Lee, H. S. van der Zant, P. G. Steeneken, and F. Alijani, Nat. Commun. **12**, 1 (2021).

[11] F. Yang, F. Hellbach, F. Rochau, W. Belzig, E. M. Weig, G. Rastelli, and E. Scheer, Phys. Rev. Lett. **127**, 014304 (2021).

[12] S. Houri, M. Asano, H. Yamaguchi, N. Yoshimura, Y. Koike, and L. Minati, Phys. Rev. Lett. **125**, 174301 (2020).

[13] A. M. Eriksson, O. Shoshani, D. López, S. W. Shaw, and D. A. Czaplewski, Nat. Commun. **14**, 161 (2023).

[14] P. Belardinelli, W. Yang, A. Bachtold, M. Dykman, and F. Alijani, Nano Lett. **25**, 8443 (2025).

[15] D. Antonio, D. H. Zanette, and D. López, Nat. Commun. **3**, 806 (2012).

[16] O. Shoshani, S. Strachan, D. Czaplewski, D. Lopez, and S. W. Shaw, Phys. Rev. Appl. **22**, 054055 (2024).

[17] L.-Q. Chen and Y. Fan, Nonlinear Dyn. **111**, 11703 (2023).

[18] K. Asadi, J. Yu, and H. Cho, Phil. Trans. R. Soc. A **376**, 20170141 (2018).

[19] A. Keşkekler, H. Arjmandi-Tash, P. G. Steeneken, and F. Alijani, Nano Lett. **22**, 6048 (2022).

[20] J. Sun, S. Yu, H. Zhang, D. Chen, X. Zhou, C. Zhao, D. D. Gerrard, R. Kwon, G. Vukasin, D. Xiao *et al.*, Phys. Rev. Appl. **19**, 014031 (2023).

[21] M. Fu, O. Ameye, F. Yang, J. Košata, J. del Pino, O. Zilberberg, and E. Scheer, Phys. Rev. Res. **7**, 033127 (2025).

[22] J. Wu, P. Song, S. Zang, Z. Mao, W. Zhang, and L. Shao, Phys. Rev. Lett. **134**, 107201 (2025).

[23] Y. Yang, E. Ng, P. Polunin, Y. Chen, S. Strachan, V. Hong, C. H. Ahn, O. Shoshani, S. Shaw, M. Dykman, and T. Kenny, in *2015 28th IEEE International Conference on Micro Electro Mechanical Systems (MEMS)* (IEEE, Estoril, Portugal, 2015), pp. 1008–1011.

[24] Y. Qiao, Z. Shi, Y. Xu, X. Wei, A. Elhady, E. Abdel-Rahman, R. Huan, and W. Zhang, Microsyst. Nanoeng. **9**, 58 (2023).

[25] Y. Fan, Y. Zhang, M.-Q. Niu, and L.-Q. Chen, Mech. Syst. Signal Process. **211**, 111176 (2024).

[26] M. Monteil, C. Touzé, O. Thomas, and S. Benacchio, Nonlinear Dyn. **75**, 175 (2014).

[27] Z. Li, M. Xu, R. A. Norte, A. M. Aragón, F. Van Keulen, F. Alijani, and P. G. Steeneken, Appl. Phys. Lett. **122**, 013501 (2023).

[28] D. Shin, A. Cupertino, M. H. de Jong, P. G. Steeneken, M. A. Bessa, and R. A. Norte, Adv. Mater. 2106248 (2022).

[29] S. A. Fedorov, A. Beccari, N. J. Engelsen, and T. J. Kippenberg, Phys. Rev. Lett. **124**, 025502 (2020).

[30] Z. Li, M. Xu, R. A. Norte, A. M. Aragón, P. G. Steeneken, and F. Alijani, Commun. Phys. **7**, 53 (2024).

[31] See Supplemental Material at http://link.aps.org/supplemental/10.1103/73wb-22pz for the details of the fabrication, measurement, modeling of mode coupling, and numerical simulation results, which includes Refs. [23,27,30,32–36].

[32] M. Xu, D. Shin, P. M. Sberna, R. van der Kolk, A. Cupertino, M. A. Bessa, and R. A. Norte, Adv. Mater. **36**, 2306513 (2024).

[33] L. G. Villanueva and S. Schmid, Phys. Rev. Lett. **113**, 227201 (2014).

[34] B. Hauer, C. Doolin, K. Beach, and J. Davis, Ann. Phys. (Amsterdam) **339**, 181 (2013).

[35] J. M. L. Miller, A. Ansari, D. B. Heinz, Y. Chen, I. B. Flader, D. D. Shin, L. G. Villanueva, and T. W. Kenny, Appl. Phys. Rev. **5**, 041307 (2018).

[36] A. H. Nayfeh and D. T. Mook, *Nonlinear Oscillations* (John Wiley & Sons, New York, 2008).

[37] Z. Li, F. Alijani, A. Sarafraz, M. Xu, R. A. Norte, A. M. Aragón, and P. G. Steeneken, Microsyst. Nanoeng. **11**, 16 (2025).

[38] S. Schmid, L. G. Villanueva, and M. L. Roukes, *Fundamentals of Nanomechanical Resonators* (Springer, New York, 2016), Vol. 49.

[39] S. Houri, D. Hatanaka, M. Asano, and H. Yamaguchi, Phys. Rev. Appl. **13**, 014049 (2020).

[40] A. A. Muravyov and S. A. Rizzi, Comput. Struct. **81**, 1513 (2003).

[41] A. Keşkekler, V. Bos, A. M. Aragón, P. G. Steeneken, and F. Alijani, Phys. Rev. Appl. **20**, 064020 (2023).

[42] A. Dhooge, W. Govaerts, Y. A. Kuznetsov, H. G. E. Meijer, and B. Sautois, Math. Comput. Model. Dyn. Syst. **14**, 147 (2008).

[43] F. Hellbach, D. De Bernardis, M. Saur, I. Carusotto, W. Belzig, and G. Rastelli, New J. Phys. **26**, 103020 (2024).

[44] M. Defoort, S. Hentz, S. W. Shaw, and O. Shoshani, Commun. Phys. **5**, 93 (2022).

[45] L. G. Villanueva, R. B. Karabalin, M. H. Matheny, E. Kenig, M. C. Cross, and M. L. Roukes, Nano Lett. **11**, 5054 (2011).

[46] X. Jin, C. G. Baker, E. Romero, N. Arora, N. P. Mauranyapin, T. M. Hirsch, G. I. Harris, and W. P. Bowen, arXiv:2509.11560.

[47] I. Mahboob and H. Yamaguchi, Nat. Nanotechnol. **3**, 275 (2008).

[48] M. Bagheri, M. Poot, M. Li, W. P. Pernice, and H. X. Tang, Nat. Nanotechnol. **6**, 726 (2011).

[49] A. Yao and T. Hikihara, Appl. Phys. Lett. **105**, 123104 (2014).